Earth, Planets and Space

FULL PAPER

Open Access

Application of the on-site P-wave earthquake early warning method based on site-specific ratios of S-waves to P-waves to the 2016 Kumamoto earthquake sequence, Japan

Seiji Tsuno[1*], Katsutomo Niwa[2], Masahiro Korenaga[1], Hiroaki Yamanaka[3], Kosuke Chimoto[4], Hiroe Miyake[5] and Nobuyuki Yamada[6]

Abstract

The on-site P-wave earthquake early warning (EEW) based on the site-specific ratios of S-waves to P-waves has been applied to large-sized offshore earthquakes, and the efficiency of the method has been validated. However, the method requires the P-waves including earthquake ground motions radiated from a large slip area while avoiding the inclusion of S-waves. In this study, we investigated the applicability of the on-site P-wave EEW method for ground motions near an earthquake source fault region, using strong-motion data observed during the 2016 Kumamoto earthquake sequence in Japan. At first, we examined the appropriate time-window length following the arrival of the P-waves. As a result, P-waves with a time-window length of 2.56 s after the arrival at most strong-motion stations were required at least to predict appropriately S-waves for the 2016 Kumamoto earthquake sequence, including the large-sized earthquakes. On the other hand, in the case of the large-sized earthquake as the mainshock (*Mj* 7.3), the method can predict within a brief time of 0.5 to 2 s in the operational use that strong ground motions exceeding a certain threshold (e.g., acceleration of 150 cm/s^2) will come. Moreover, we found that the method was not strongly affected by the non-linearity of soil deposits due to strong ground motions during the 2016 Kumamoto earthquake sequence. The variability of the relationship between P- and S-waves at the seismic bedrock influenced by the source and path effects is larger than the variability of the relationships between P-/S-waves at the seismic bedrock and at the ground surface by the site effects, and therefore, it hides the effect of the non-linearity of soil deposits.

Keywords On-site EEW, P-wave, Site-specific ratio, Data length, Earthquake source fault region, Non-linearity, The 2016 Kumamoto earthquake sequence

*Correspondence:
Seiji Tsuno
tsuno.seiji.75@rtri.or.jp
Full list of author information is available at the end of the article

Graphical Abstract

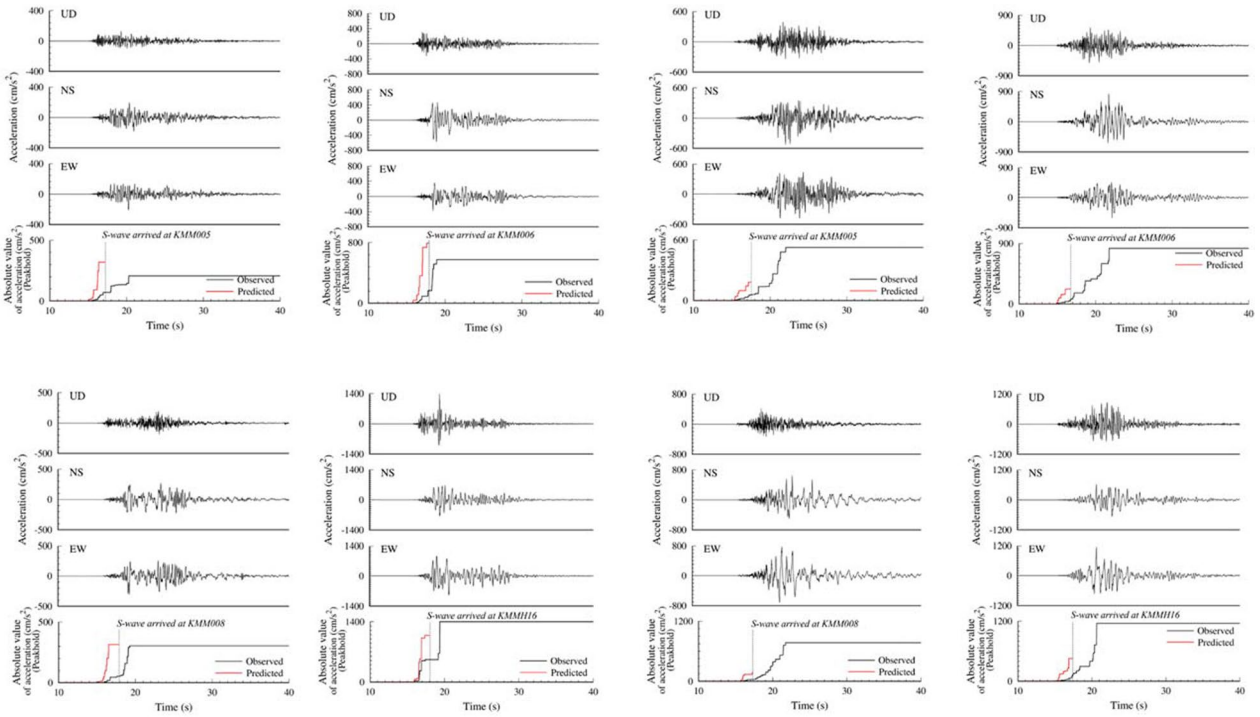

Introduction

On-site earthquake early warning (EEW) systems estimate the strength of ground shaking at the same location using a beginning part immediately after the arrival of P-waves (Nakamura 1988; Allen and Kanamori 2003; Odaka et al. 2003; Wu and Kanamori 2005; Wu et al. 2007; Okamoto and Tsuno 2015). The EEW systems are globally installed in many fields based on their own concepts to provide a warning prior to the strength of ground shaking (Allen et al. 2009). Recently, methods reflecting differences at sites in the strength of ground shaking based on empirical site characteristics have been developed (Miyakoshi and Tsuno 2015; Miyakoshi et al. 2019; Tsuno and Miyakoshi 2019; Zhao and Zhao 2019; Tsuno 2021). Tsuno (2021) applied the EEW method based on the empirical spectral ratio of S-wave to P-wave to seismic data of the 2011 off the Pacific coast of Tohoku earthquake (Mw 9.0), as large-sized offshore earthquakes. However, the performance and accuracy of these methods when applied to large-sized inland earthquakes have not yet been investigated.

A sequence of earthquakes occurred on April 14 (*Mj* 6.5) and April 16 (*Mj* 7.3) 2016 in the Kumamoto Prefecture, Japan (e.g., Asano and Iwata 2016) and induced destructive strong ground motions. In particular, the town of Mashiki, where a 7 on the Japanese seismic intensity scale was recorded, experienced heavy earthquake damage to buildings. Since the earthquake, much research on strong ground motions, nonlinear behaviors of subsurface soil, and earthquake damage has been undertaken in this area (e.g., Chimoto et al. 2016; Kawase et al. 2017; Yamanaka et al. 2016; Yamada et al. 2017; Sun et al. 2021, 2022). Yamanaka et al. (2016) installed temporary seismic stations near the earthquake source fault region immediately after the mainshock of the 2016 Kumamoto earthquake, which occurred on April 16, 2016, whereas Tsuno et al. (2017) installed temporary seismic stations in Kumamoto City immediately after the foreshock, which occurred on April 14, 2016. Yamanaka et al. (2016) recorded strong-motion data with highly dense arrays located in the earthquake source fault region, and Tsuno et al. (2017) recorded in the Kumamoto Plain consisting of the diluvial plateau and alluvial lowland (Hoshizumi et al. 2004; Ishizaka et al. 1995).

In this study, we focused on the performance and accuracy of the on-site P-wave EEW method based on

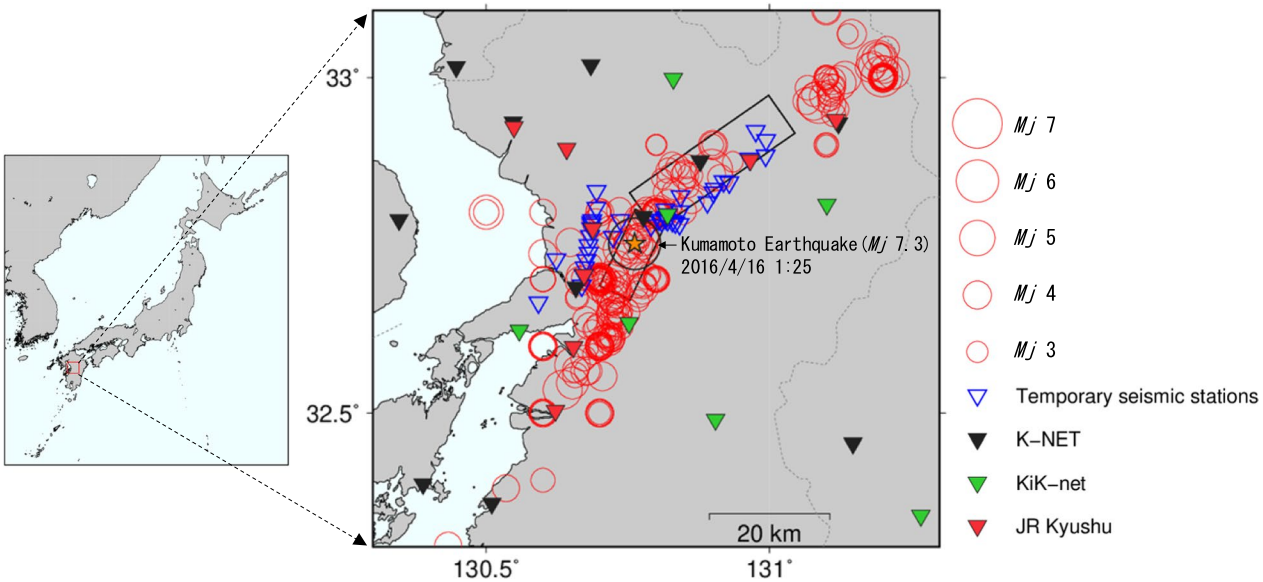

Fig. 1 Locations of epicenters and strong-motion stations in Kumamoto region, Japan used in this study. Red circles denote epicenters of the 2016 Kumamoto earthquake sequence with magnitudes. A star with a black circle denotes an epicenter of the mainshock. Inverse triangles denote strong-motion stations of K-NET, KiK-net, and JR Kyushu, and temporary seismic stations. Temporary seismic stations were installed by Yamanaka et al. (2016) and Tsuno et al. (2017). Source fault planes of the mainshock by Asano and Iwata (2016) are projected with black rectangles

the site-specific ratio proposed by Tsuno (2021), using strong-motion data from the 2016 Kumamoto earthquake sequence. Finally, the applicability of this method to strong-motion data from the foreshock, mainshock, and largest aftershock of the 2016 Kumamoto earthquake sequence in the operational use was investigated.

Data

We used strong-motion data of foreshocks, mainshock, and aftershocks of the 2016 Kumamoto earthquake sequence, obtained from strong-motion networks of K-NET (Kinoshita 1998) and KiK-net operated by the NIED (National Research Institute for Earth Science and Disaster Resilience, 2019b), and from a strong-motion network of Japan Railways, the Kyushu Railway Company. In addition, we used strong-motion data from temporary seismic stations near the earthquake source fault region installed by Yamanaka et al. (2016) immediately after the mainshock of the Kumamoto earthquake, which occurred on April 16, 2016, and from temporary seismic stations in Kumamoto City installed by Tsuno et al. (2017) immediately after the foreshock of the earthquake, which occurred on April 14, 2016. The locations of the epicenters and strong-motion stations used in this study are shown in Fig. 1, while Fig. 2 shows the magnitude and depth of the earthquakes. Figure 3 shows the histograms of the epicentral distance and the maximum acceleration for the earthquake datasets recorded at all stations shown in Fig. 1. The datasets include data from earthquakes with a magnitude (Mj) of 2.5–7.3 and a depth of 0 to 25 km. Epicentral distance from strong-motion stations

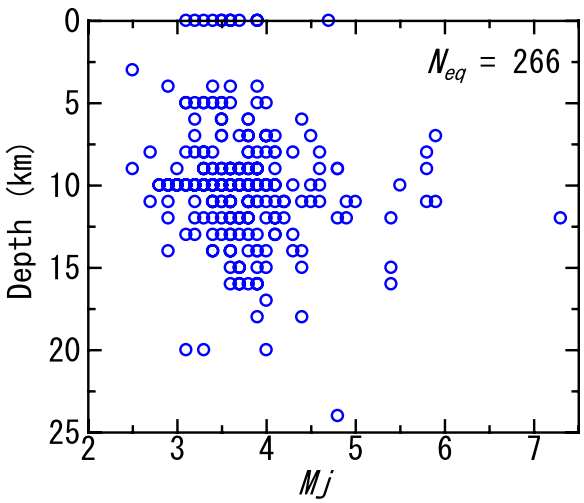

Fig. 2 Magnitudes and depths of earthquakes shown in Fig. 1. N_{eq} indicates the number of earthquakes used in this study

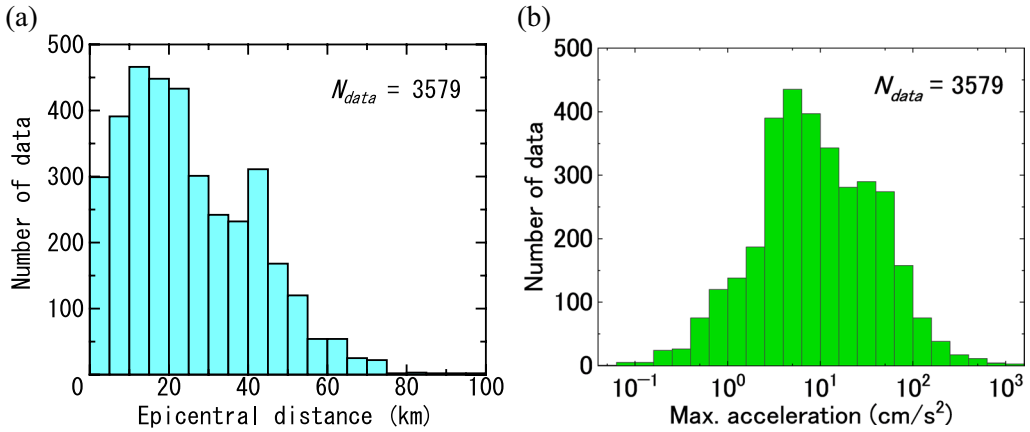

Fig. 3 Histograms of the epicentral distance (**a**) and the maximum acceleration (**b**) for earthquake datasets recorded at all the stations shown in Fig. 1. N_{data} indicates the number of earthquake datasets recorded at all the stations used in this study

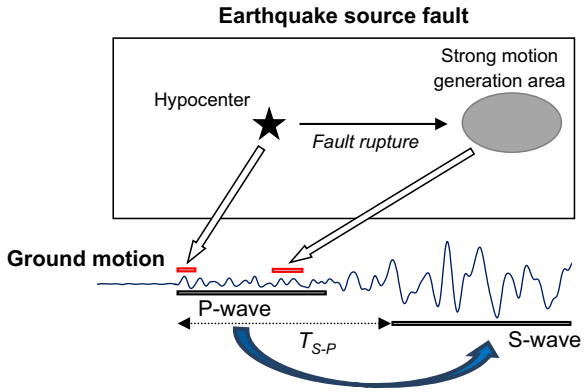

Fig. 4 Conceptual diagram of the on-site P-wave EEW method applied to strong-motion data near an earthquake source fault region

was mostly within 30 km, and most of the maximum accelerations were less than 10 cm/s^2.

On-site P-wave EEW method based on the site-specific ratio of S-wave to P-wave

Method

A conceptual diagram of the on-site P-wave EEW method is shown in Fig. 4. The method directly predicts S-waves by multiplying site-specific ratios of S-waves to P-waves with P-waves observed in real-time at a strong-motion station, as expressed by Eq. (1) in the frequency domain with a logarithm (Tsuno and Miyakoshi 2019; Tsuno 2021). The method using P-waves can significantly reduce the time difference between the arrivals of P- and S-waves (T*s-p*) to issue warnings compared to previous methods that mainly use S-waves. Equations (1)–(3) are derived by assuming an earthquake ground motion observed in a far field induced by a double-couple point source:

$$\log O_{\mathrm{s}}^{S}(\omega) = \log O_{\mathrm{s}}^{P}(\omega) + b(\omega), \tag{1}$$

$$b(\omega) = a_1(\omega) - a_2(\omega) + a_3(\omega), \tag{2}$$

$$a_1(\omega) = \log \frac{V_{\mathrm{P}}^3}{V_{\mathrm{S}}^3} + \log \frac{R_{\theta\varphi}^{S}}{R_{\theta\varphi}^{P}} + \log e^{\frac{r\omega}{2}\left(-\frac{1}{Q_{\mathrm{S}}V_{\mathrm{S}}'}+\frac{1}{Q_{\mathrm{P}}V_{\mathrm{P}}'}\right)},$$
$$a_2(\omega) = \log G^{P}(\omega),\ a_3(\omega) = \log G^{S}(\omega). \tag{3}$$

Here, O represents the earthquake motion; ω represents the angular frequency; V is the velocity of the body waves in and around the earthquake source region (e.g., Matsubara and Obara 2011); r is the distance from the earthquake source; $R_{\theta\phi}$ is the radiation coefficient; Q represents the intrinsic attenuation of the crust; V' is the average velocity of the body waves in the crust (e.g., Matsubara et al. 2005); and G represents the transfer function of a subsurface structure from the basement (seismic bedrock) to the ground surface at a site. The subscripts P and S represent P-waves and S-waves, respectively. Finally, the subscripts of s represents the ground surface.

In practice, $b(\omega)$ that is estimated from the spectral ratios of the S-waves to the P-waves using strong-motion data observed on the ground surface at a site, is affected by the source, path, and site effects (Tsuno and Miyakoshi 2019). $a_1(\omega)$ includes the source and path effects, and $a_2(\omega)$ and $a_3(\omega)$ include the site effects that are the transfer functions of P-waves and S-waves, respectively.

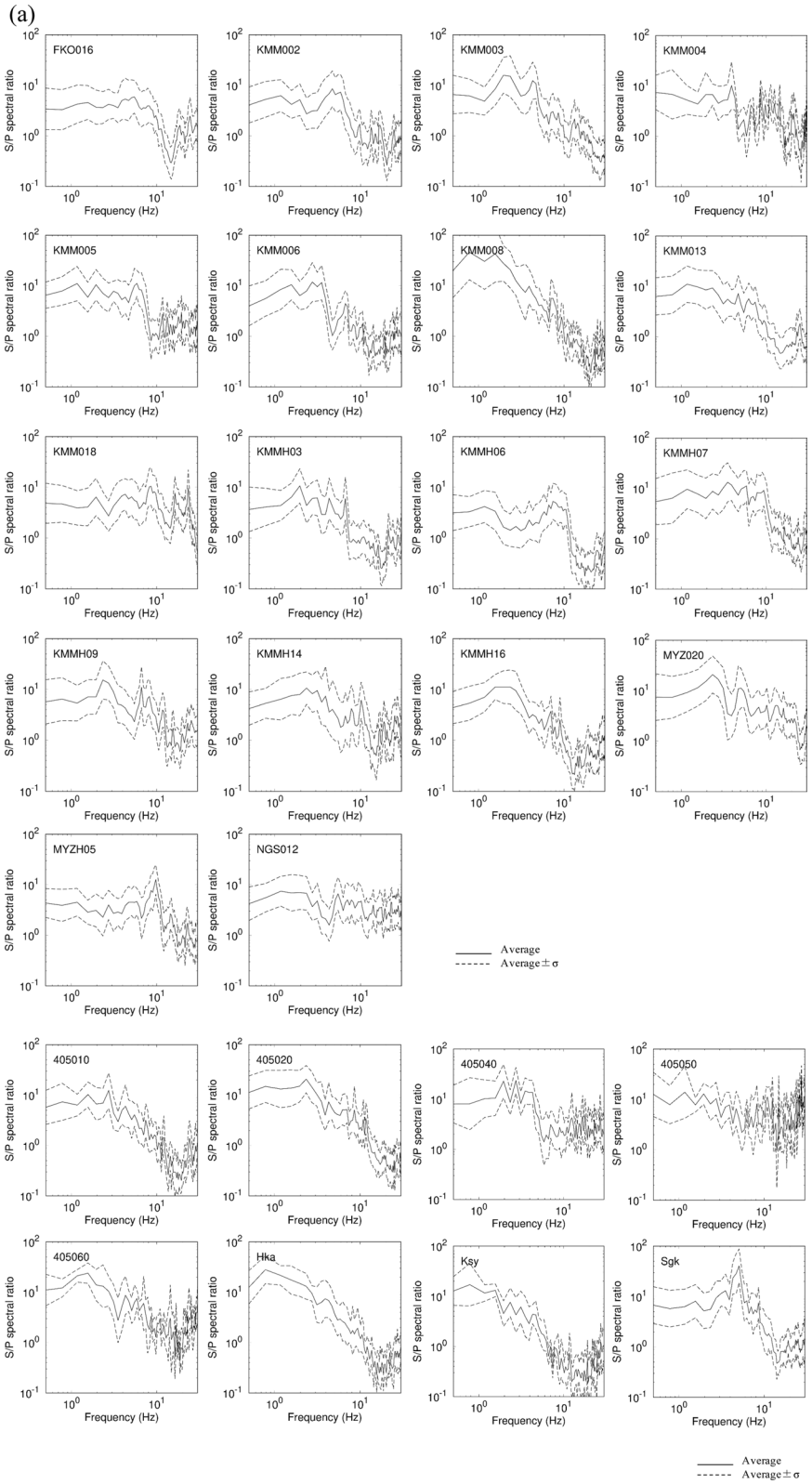

Fig. 5 Estimated site-specific average spectral ratios of S-waves to P-waves using a time-window of 2.56 s at the strong-motion stations with the standard deviations. **a** Strong-motion stations of K-NET, KiK-net, and JR Kyushu. **b** Temporary seismic stations

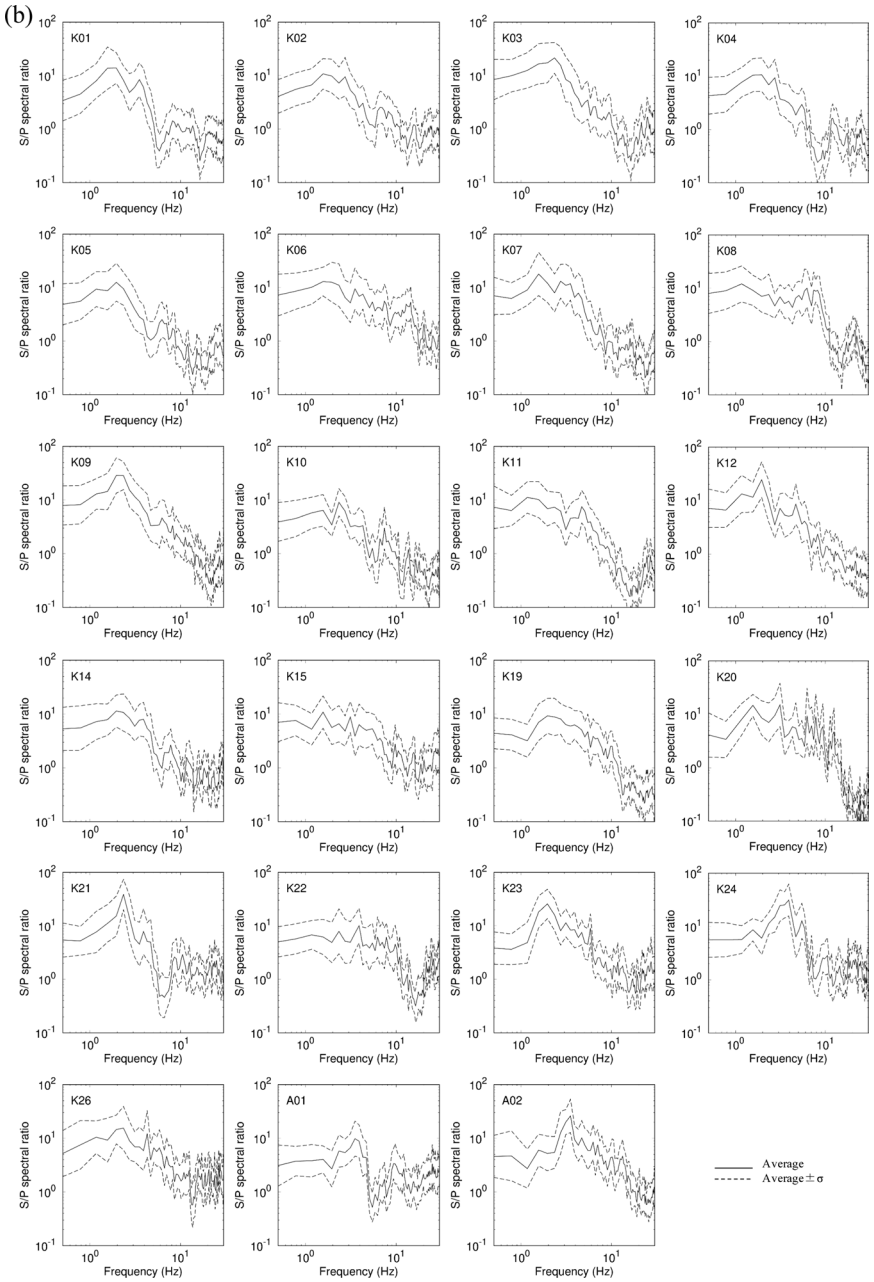

Fig. 5 continued

Miyakoshi and Tsuno (2015) investigated the relationship between P-waves at the seismic bedrock and S-waves at the ground surface using theoretical techniques, empirical formulas, and observational data. As a result, Miyakoshi and Tsuno (2015) concluded that the spectral ratios of the S-waves at the ground surface to the P-waves at the seismic bedrock were significantly affected by the site effects, in contrast to the source and path effects. For

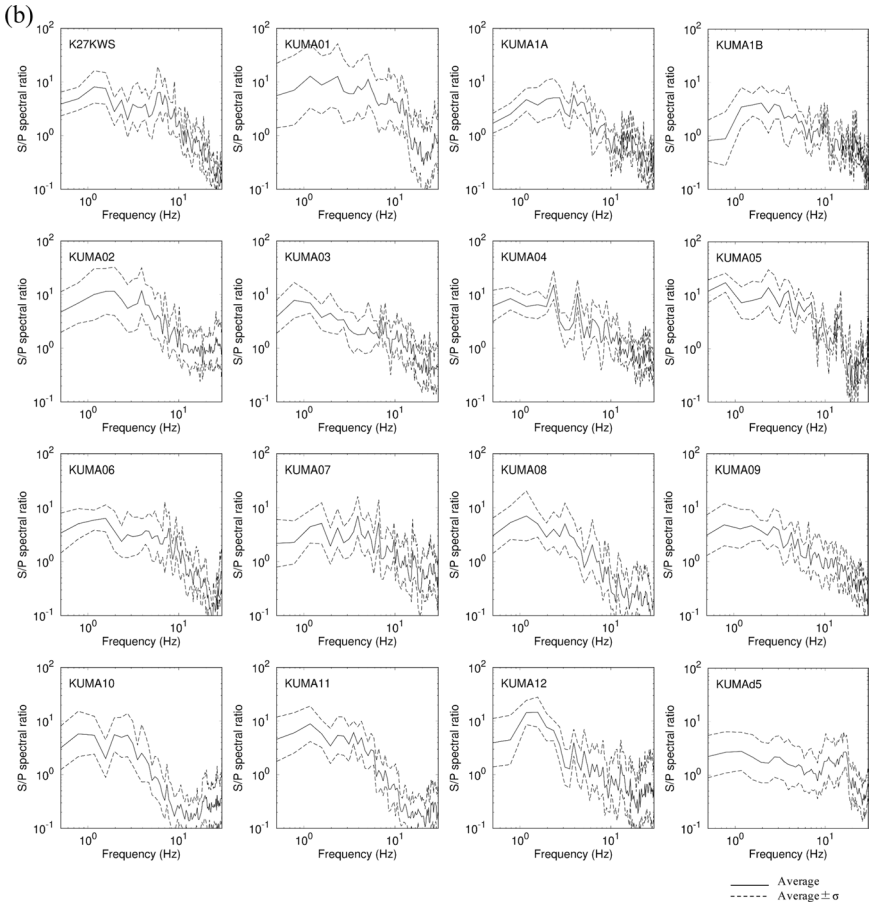

Fig. 5 continued

peak ground motions, the method is applied by replacing the value in the frequency domain with the maximum value in the time domain, such as PGA (peak ground acceleration) and PGV (peak ground velocity).

Issue of the on-site P-wave EEW method applied to strong-motion data near an earthquake source fault region

We need to investigate an appropriate time-window length following the arrival of the P-waves because the on-site P-wave EEW method requires including the P-wave seismic phases radiated from a large slip area (Fig. 4). Moreover, this method should be applied to P-waves only by carefully avoiding the inclusion of S-waves, especially for strong-motion data near an earthquake source fault region. This study therefore quantitatively investigated the performance of the method by applying short time-window lengths of P-waves, using the strong-motion data of the 2016 Kumamoto earthquake sequence, Japan.

Site-specific ratio of S-wave to P-wave

We estimated site-specific spectral ratios of S-waves to P-waves for the Fourier spectrum and site-specific ratios of S-waves to P-waves for PGA using data observed at the strong-motion stations during the 2016 Kumamoto earthquake sequence. First, the onsets of P-waves and S-waves for all data were visually read. The Fourier spectra of S-waves in the horizontal components and P-waves in the vertical component without a smoothing process were calculated using a time-window of 2.56 s after the onsets. The time of Ts-p in the strong-motion data was sufficiently secured to avoid mixing the S-waves into a part of the P-waves. The spectral ratios of the S-waves to the P-waves were estimated by dividing the Fourier amplitude spectra of the S-waves which is the arithmetic mean of the NS and EW components by that of the P-waves of the UD component. Finally, the spectral ratios of the S-waves to the P-waves were averaged by those for all strong-motion data recorded at each strong-motion station. For the site-specific ratios of the S-waves to the

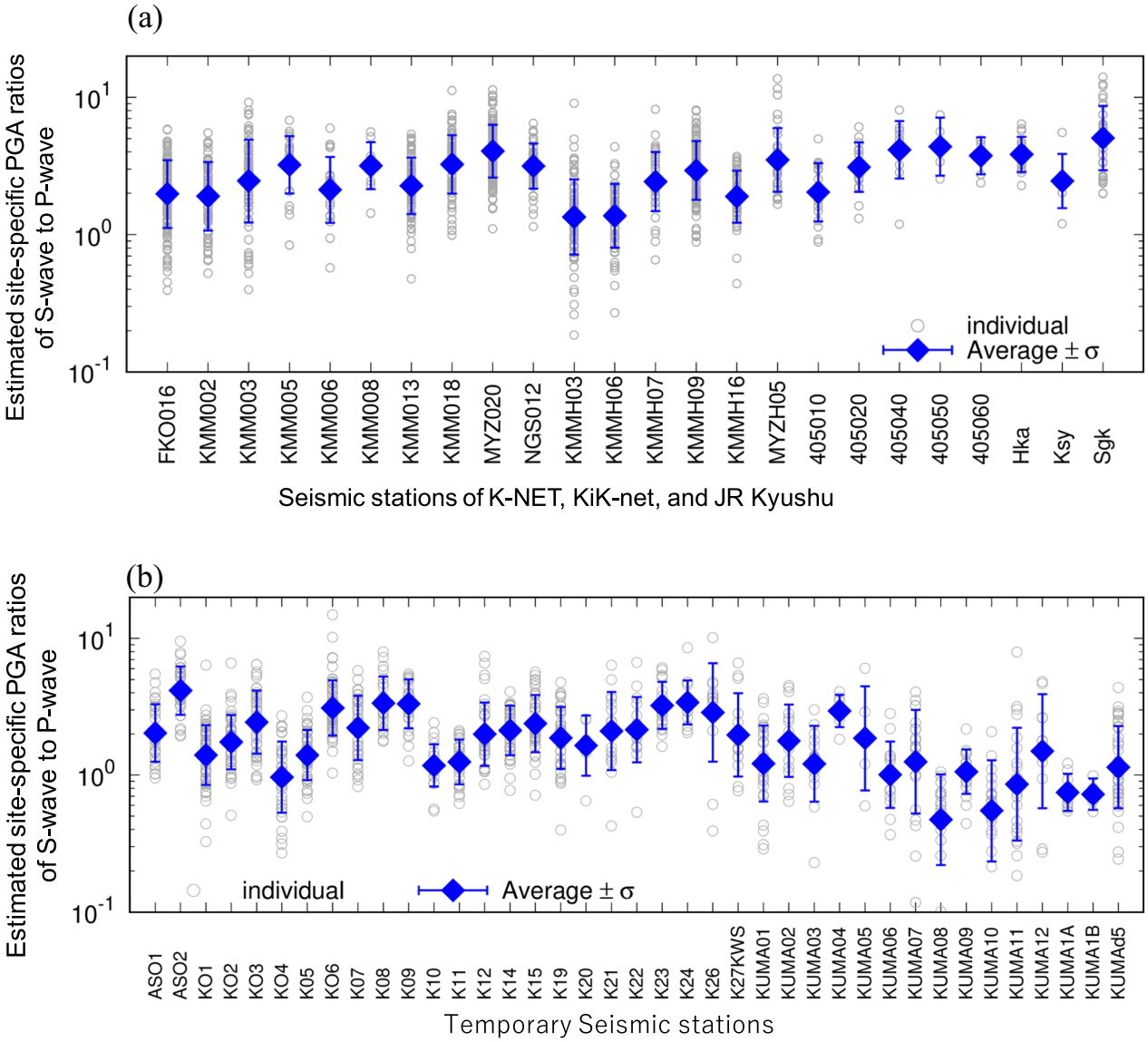

Fig. 6 Estimated site-specific average ratios of S-waves to P-waves for PGA using a time-window of 2.56 s at the strong-motion stations with the standard deviations. **a** Strong-motion stations of K-NET, KiK-net, and JR Kyushu. **b** Temporary seismic stations

P-waves for PGA, the same processing as the Fourier spectrum was performed.

The estimated site-specific spectral ratios of S-waves to P-waves using a time-window of 2.56 s at the strong-motion stations of K-NET/KiK-net and JR Kyushu, and the temporary seismic stations are shown in Fig. 5. The site-specific spectral ratios of S-waves to P-waves are greater than 1 in the frequency range less than 5 Hz at most strong-motion stations due to the influence of the transfer functions of $a_3(\omega)$ by S-wave velocity structures at each site, as shown in Eq. (3). In contrast, the site-specific spectral ratios of the S-waves to the P-waves are less than 1 in the frequency range of more than 10 Hz at most strong-motion stations due to the influence of the transfer functions of $a_2(\omega)$ by the P-wave velocity structures at each site, as shown in Eq. (3). The estimated site-specific ratios for PGA at the strong-motion stations of K-NET/KiK-net and JR Kyushu, and the temporary seismic stations are shown in Fig. 6. The spatial distribution of the estimated site-specific ratios for PGA is shown in Fig. 7. Accelerations of earthquake ground motion are generally amplified by the site effects at high frequencies of several hertz; therefore, the averaged site-specific ratios for PGA are greater than 1. In particular, site-specific ratios

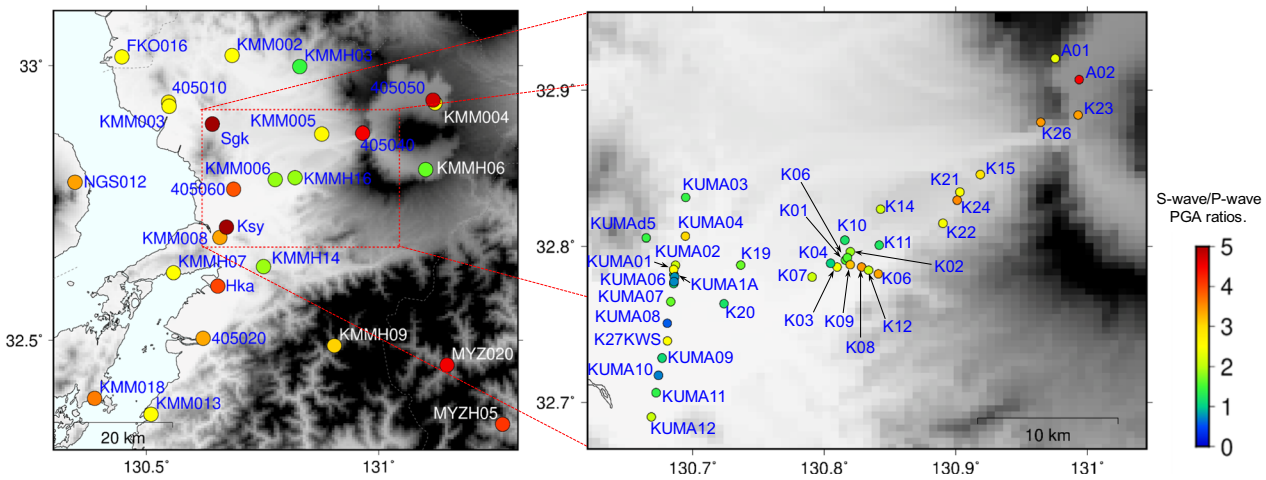

Fig. 7 Spatial distribution of the estimated site-specific ratios of S-waves to P-waves for PGA at the strong-motion stations

for PGA have a large amplification at rock sites such as MYZ020 and MYZH05 shown in Fig. 7, due to the thin surface soil deposited on the bedrock in the mountain by J-SHIS (NIED, 2019a). The site-specific ratios for PGA at each site varied several times or more at a local spatial scale as well as at a larger special scale (see Fig. 7), indicating the importance of evaluating individual site characteristics.

Prediction of S-wave in real-time

We predicted S-waves by multiplying the site-specific spectral ratios of S-waves to P-waves prepared in advance by P-waves observed in real-time at each strong-motion station. As expressed in the previous section, the time-window to estimate the site-specific spectral ratios of S-waves to P-waves was 2.56 s. To investigate the accuracy of the predicted S-waves by using different time-window lengths of P-waves, on the other hand, time-window lengths of P-waves observed in real-time were varied as 0.64, 1.28, and 2.56 s. As an example, Fig. 8 shows the Fourier amplitude spectra of S-waves predicted by the method for the earthquake of *Mj* 5.8, which occurred on April 18, 2016, at the strong-motion stations of K-NET/KiK-net and JR Kyushu, and the temporary seismic stations. Results show that the accuracy of the S-wave prediction increases as the time-window length of the P-wave increases. When the time-window length of the P-waves was 2.56 s, the predictions of the Fourier amplitude spectra of the S-waves corresponded with observations at most strong-motion stations. The PGAs of the S-waves predicted for all earthquakes in a time of T*s-p* more than 2.56 s at the strong-motion stations are shown in Fig. 9. The predictions of the PGAs of the S-waves were in good agreement with the observations at most strong-motion stations, within a standard deviation of 0.3. This indicates that the on-site P-wave EEW method based on the site-specific spectral ratios of S-waves to P-waves can predict the observed S-waves in the single indicator of PGA as well as in the frequency content, using a sufficient time-window length of the P-waves.

Investigation of time-window length of P-wave

We investigated an appropriate time-window length from the arrival of the P-waves using earthquake ground motion data of the 2016 Kumamoto earthquake sequence. The predicted PGAs of the S-waves using different time-window lengths from the arrival of P-waves for all earthquakes at the strong-motion stations are shown in Fig. 10. In the figure, standard deviation σ and coefficient determination R^2 in logarithm are also indicated. Clearly, the accuracy of the S-wave prediction increases as the time-window length from the arrival of P-waves increases in the datasets. Residual standard deviations between the observations and the predictions for PGAs of S-waves against time-window lengths from the arrival of P-waves at the strong-motion stations are shown in Fig. 11. The residual standard deviations start to be stable over time-window lengths of around 1.5 s from an arrival of P-wave with a value of 0.3, even though the value of 0.4 for time-window lengths of around 0.5 s is not high. In general, a long P-wave time-window length is not necessary for a small earthquake due to the limited rise time of earthquake fault rupture. The residual standard deviations for earthquakes of *Mj* 4 or larger and earthquakes of *Mj* less than 4 are shown in Fig. 12. These

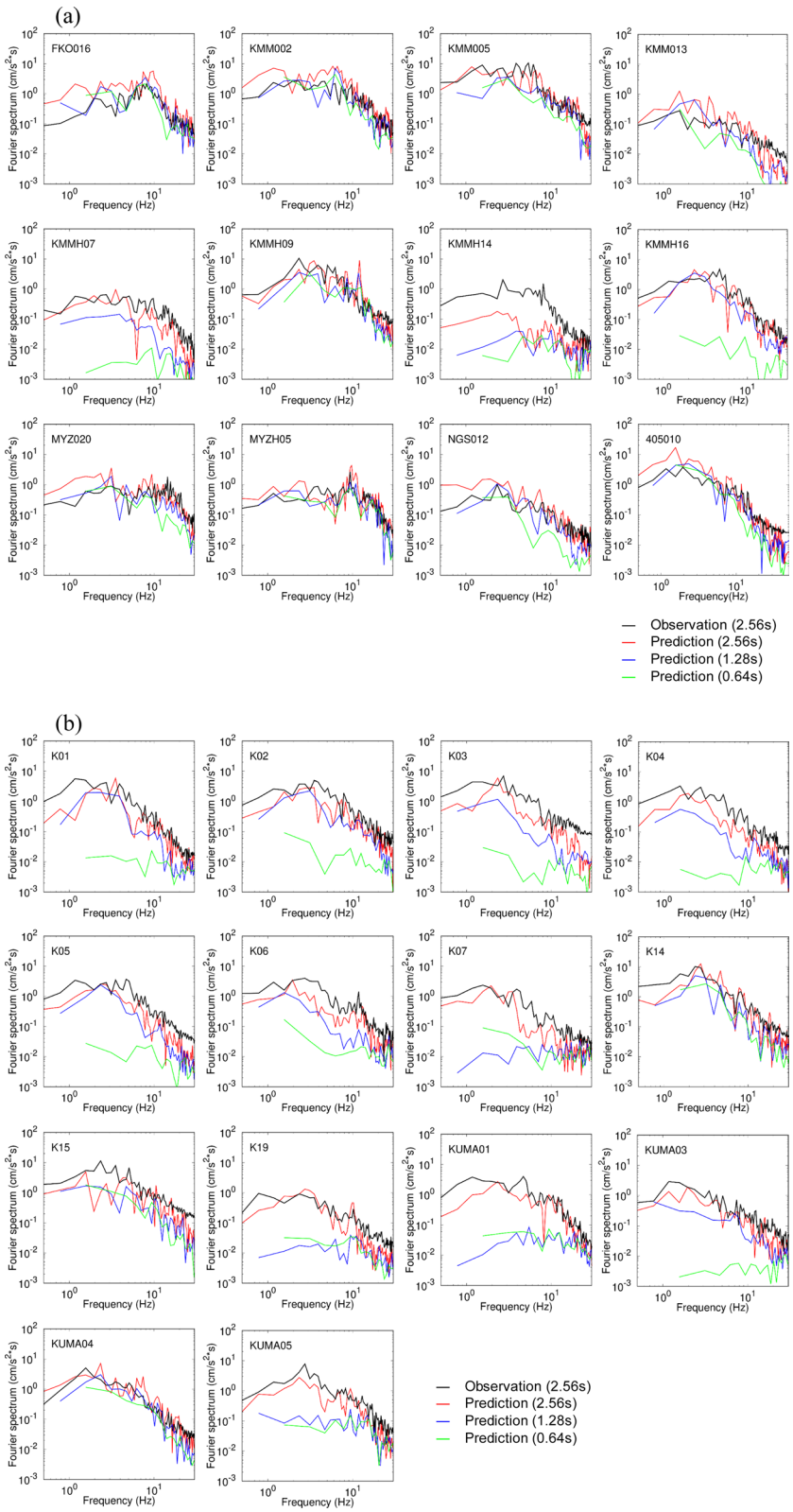

Fig. 8 Predicted Fourier amplitude spectra of S-waves for the earthquake of *Mj* 5.8 on April 18, 2016 at the strong-motion stations. Different time-window lengths of 0.64, 1.28, and 2.56 s of P-waves observed in real-time were used. **a** Strong-motion stations of K-NET, KiK-net, and JR Kyushu. **b** Temporary seismic stations

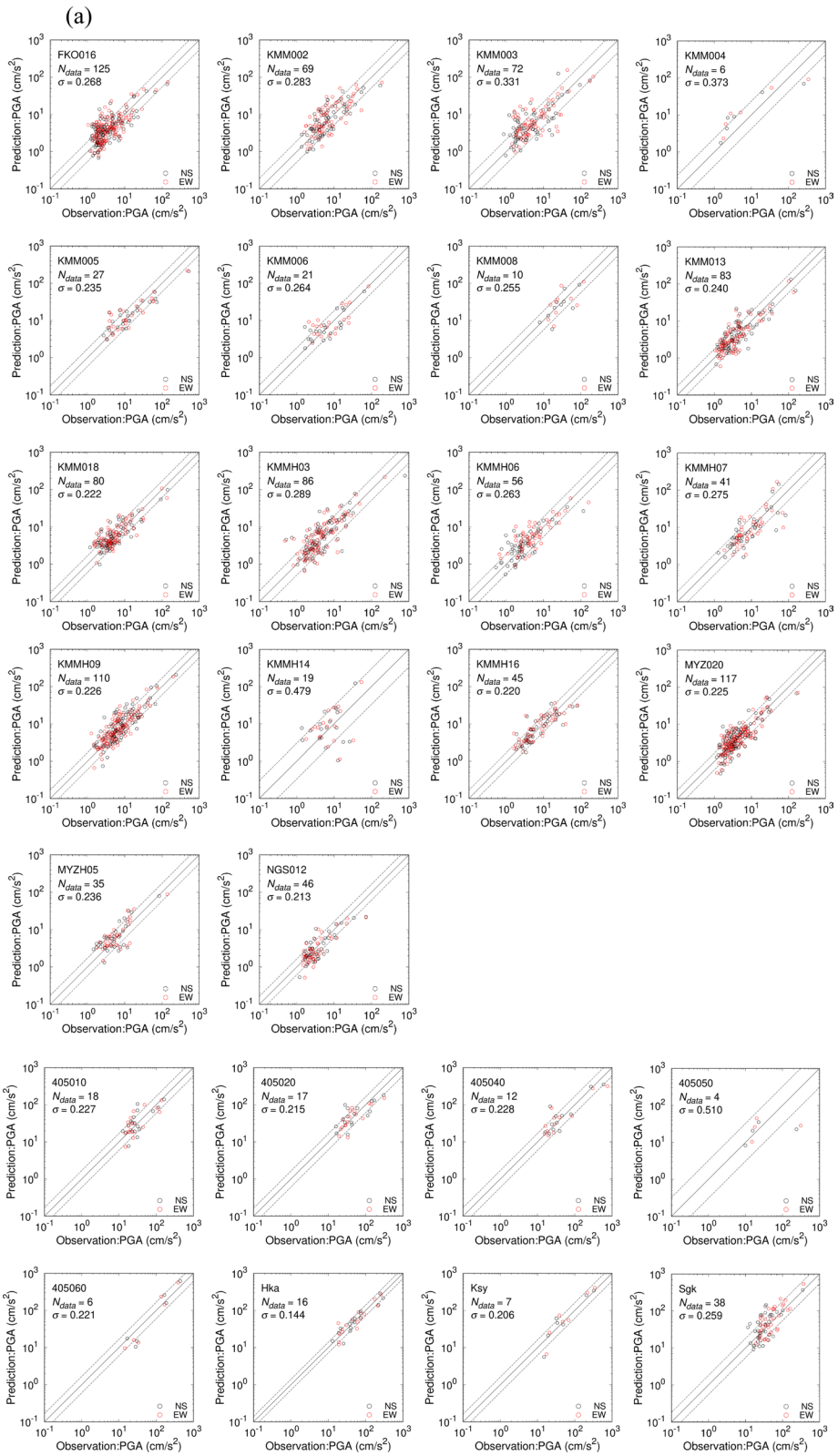

Fig. 9 Predicted PGAs of S-waves for all the earthquakes in a time of T*s-p* more than 2.56 s at the strong-motion stations with the standard deviations. N_{data} indicates the number of earthquakes recorded. **a** Strong-motion stations of K-NET, KiK-net, and JR Kyushu. **b** Temporary seismic stations

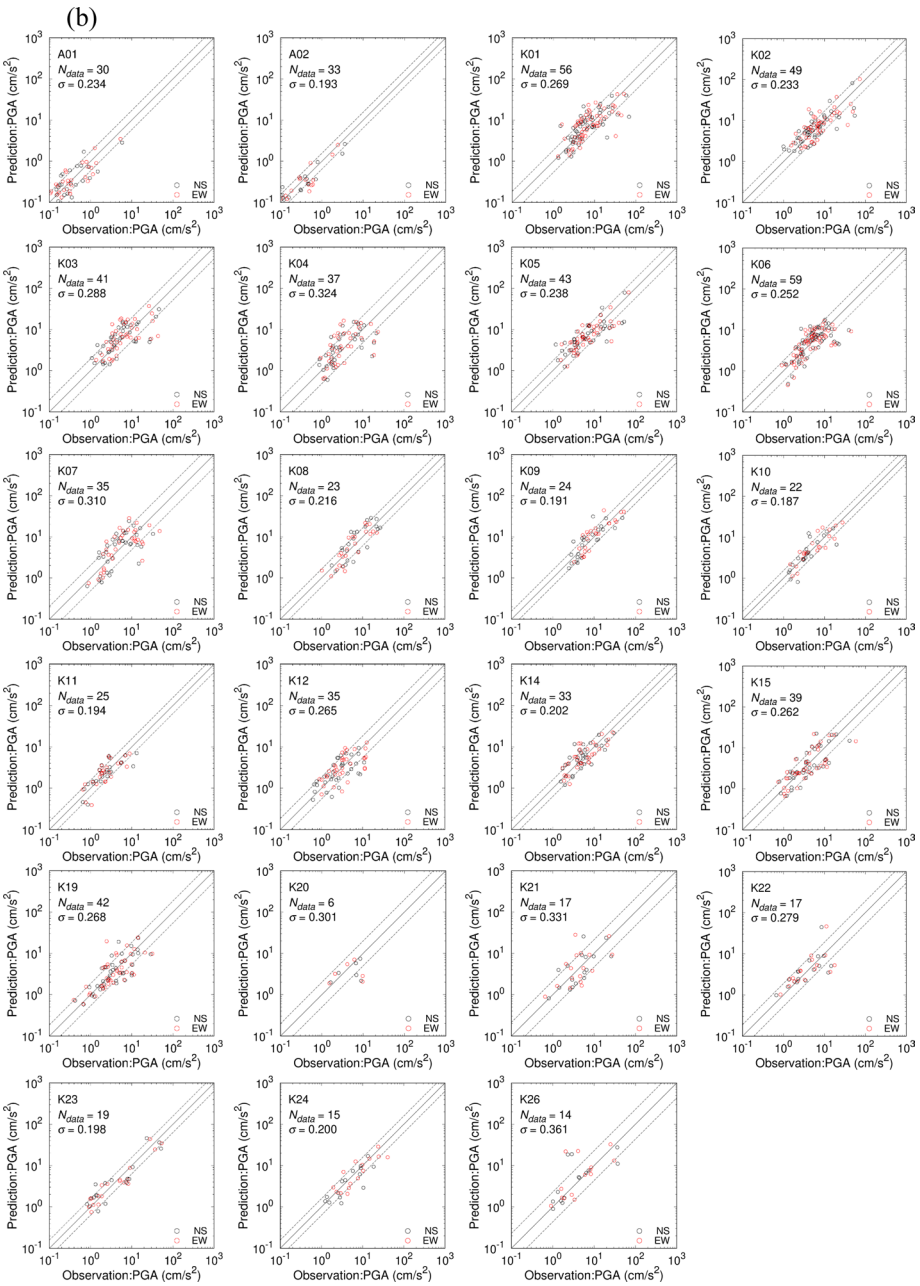

Fig. 9 continued

figures indicate that a longer time-window length for the P-wave is generally required for large earthquakes than for small earthquakes.

Applications to the 2016 Kumamoto earthquake sequence

We applied the method to the mainshock data of the 2016 Kumamoto earthquake observed at the strong-motion stations of K-NET, KiK-net, and JR Kyushu, and temporary seismic stations. Figures 13 and 14 show Fourier amplitude spectra and PGAs of S-waves for the mainshock strong-motions predicted by different time-window lengths from the arrival of P-waves, respectively. The predictions by time-window lengths of 0.64 and 1.28 s clearly underestimated the observations. In contrast, the predictions by a time-window length of 2.56 s slightly underestimated the observations in the results of PGAs, as well as the results of Fourier spectra. To appropriately predict the S-waves for the

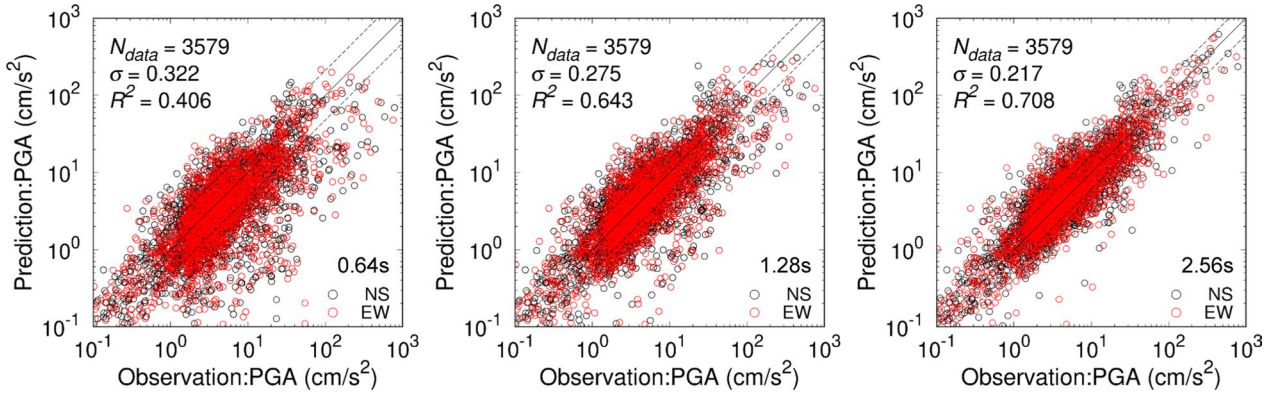

Fig. 10 Predicted PGAs of S-waves using different time-window lengths from P-waves arrival for all the earthquakes at the strong-motion stations. In the figure, standard deviation σ and coefficient determination R^2 in logarithm are indicated. N_{data} indicates the number of earthquake datasets recorded at all the stations

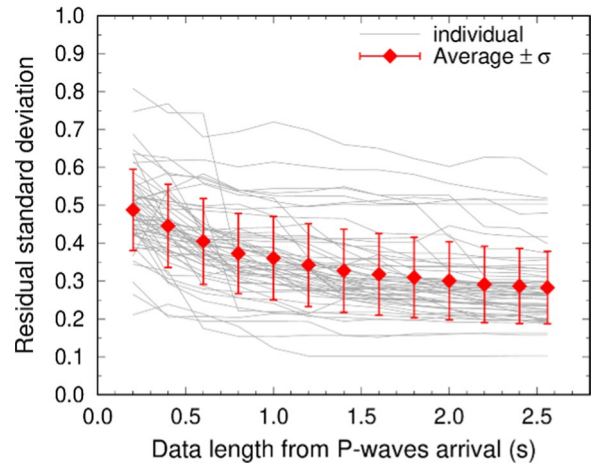

Fig. 11 Residual standard deviations between the observations and the predictions for PGAs of S-waves against time-window lengths from P-waves arrival at the strong-motion stations. In the figure, standard deviation σ in logarithm is indicated

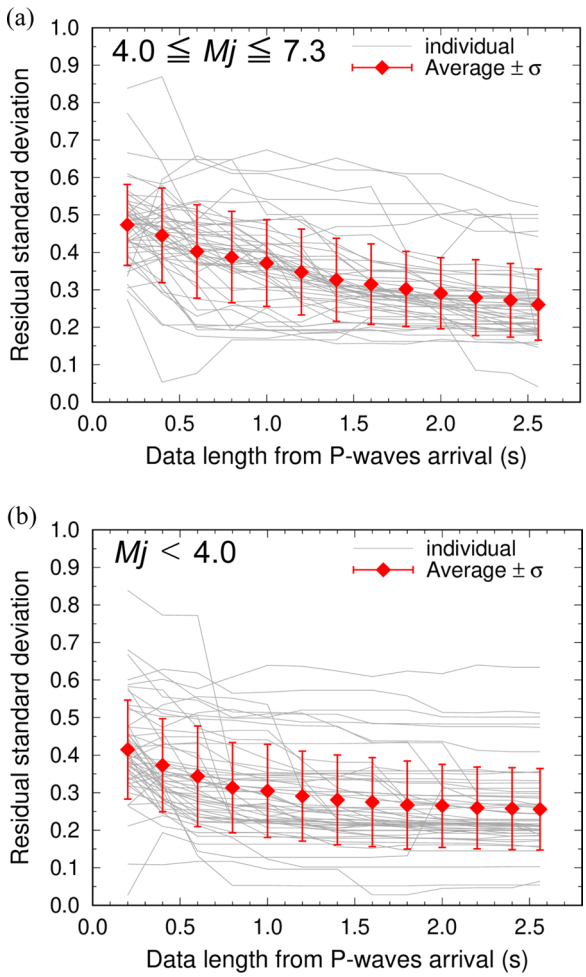

Fig. 12 Residual standard deviations between the observations and the predictions for PGAs of S-waves against time-window lengths from P-waves arrival, for earthquakes of *Mj* 4 or larger and earthquakes of less than *Mj* 4, at the strong-motion stations. In the figure, standard deviation σ in logarithm is indicated. **a** Earthquakes of than *Mj* 4 or larger. **b** Earthquakes of less than *Mj* 4

mainshock of the 2016 Kumamoto earthquake, a time-window length of more than 2.56 s from the arrival of the P-waves is needed, caused by the large earthquake magnitude (*Mj* 7.3). In the case of the prediction of PGA with a time-window length of 5.12 s, predictions larger than 500 cm/s^2 overestimated the observations due to the inclusion of the S-waves at some strong-motion stations. The method presented here approximately predicts S-waves for the mainshock of the 2016 Kumamoto earthquake at most strong-motion stations near the earthquake source fault region, using an appropriate time-window length of more than 2.56 s from P-waves arrival. As a result of Asano and Iwata (2016), the large slip area for the mainshock is mainly

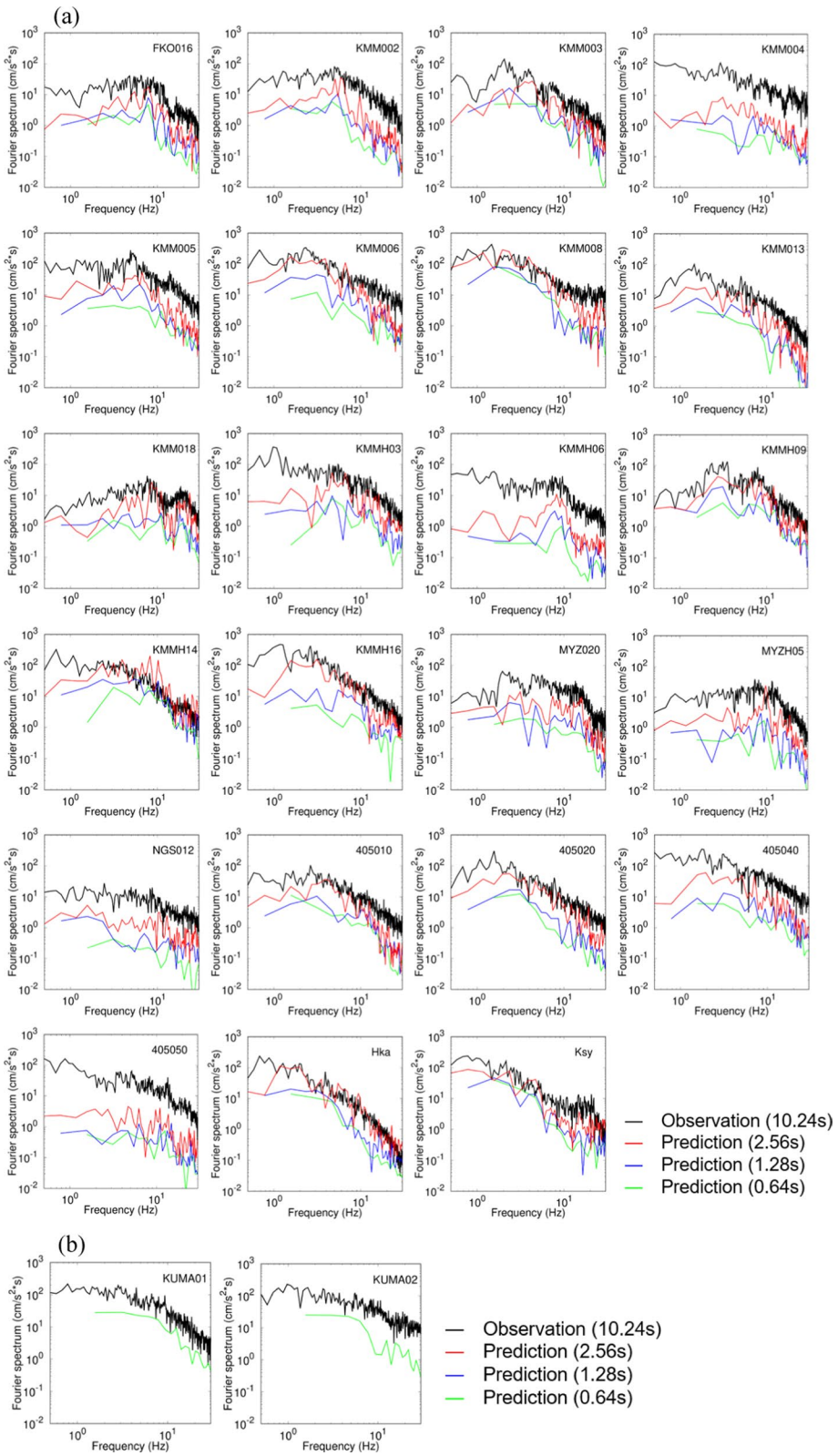

Fig. 13 Fourier amplitude spectra of S-waves for the mainshock of the 2016 Kumamoto earthquake at the strong-motion stations of K-NET, KiK-net, and JR Kyushu, and temporary seismic stations predicted by different time-window lengths from the P-waves arrival. **a** Strong-motion stations of K-NET, KiK-net, and JR Kyushu. **b** Temporary seismic stations

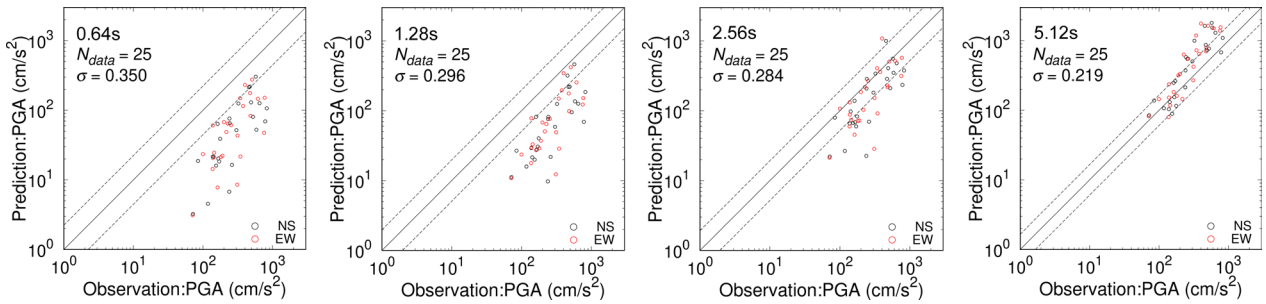

Fig. 14 PGAs of S-waves for the mainshock of the 2016 Kumamoto earthquake at the strong-motion stations of K-NET, KiK-net, and JR Kyushu, and temporary seismic stations predicted by different time-window lengths from the P-waves arrival. N_{data} indicates the number of earthquakes recorded. In the figure, standard deviation σ in logarithm is indicated

about 4 km × 2 km with the main part of the rise time of about 3 s. It is the reason that a duration of 2.56 s was suitable for predicting strong ground motions during the mainshock of the 2016 Kumamoto earthquake by the proposed method, even though ground motions are slightly underpredicted.

In real-time, absolute values of accelerations (Peak-hold) by multiplying the site-specific ratios prepared in advance (see Fig. 6) by absolute values of accelerations of P-waves observed were predicted for the foreshock, mainshock, and largest aftershock of the 2016 Kumamoto earthquake sequence. The predicted and observed absolute values of accelerations of S-waves at KMM005, KMM006, KMM008, and KMMH16 which are located near the earthquake source fault region of the mainshock, with the observed accelerations in 3 components during foreshock (21:26 on April 14, *Mj* 6.5), mainshock (1:25 on April 16, *Mj* 7.3), and largest aftershock (1:45 on April 16, *Mj* 5.9) of the 2016 Kumamoto earthquake sequence are shown in Fig. 15. In the figure, the predicted absolute values of accelerations of S-waves by the method are shown with the sampling frequency of 100 Hz until the time that S-waves arrive at each station (e.g., Allen 1978; Morita and Hamaguchi 1981). The predicted absolute values of accelerations of S-waves are gradually and/or sharply increasing until S-waves arrive at each station. The predicted absolute values of accelerations immediately before S-waves arrival reproduced the maximum values of S-waves observed at stations within a half and twice accuracy for the foreshock and largest aftershock, as shown in Fig. 15a and c. In cases of moderate-sized earthquakes as the foreshock and largest aftershock, the proposed method can predict well the observed absolute accelerations despite the brief time until S-waves arrive at each station, mostly less than two seconds. On the other hand, the predicted absolute values of accelerations underestimated the maximum values of S-waves observed at stations for the mainshock as shown in Fig. 15b. In the case of large-sized earthquakes as the mainshock, the proposed method could not adequately predict the observed absolute accelerations in a brief time until S-waves arrive at each station. It is caused by that the strong ground motions radiated from the large slip area are not sufficiently included in the P-waves until the arrival of S-waves near the earthquake source fault region. We found out that the proposed method efficiently plays a role in taking the lead time of several seconds until the maximum values of S-waves arrive even at stations near the earthquake source fault region and can contribute to an earthquake early warning in the case of the mainshock of the 2016 Kumamoto earthquake.

Discussion

Strong ground motions observed on the ground surface are frequently accompanied by the non-linearity of soil deposits (e.g., Field et al. 1998). Therefore, we need to investigate the performance of the proposed method for strong ground motions with the non-linearity of soil deposits. During the mainshock of the 2016 Kumamoto earthquake, strong ground motions with a PGA larger than 300 cm/s^2 were widely observed in and around the earthquake source fault region (Suzuki et al. 2017). Non-linearity and liquefaction of soil deposits during the mainshock of the 2016 Kumamoto earthquake were reported (e.g., Tsuno et al. 2017; Wakamatsu et al. 2017; Sun et al. 2022). Sun et al. (2022) reported that there are several sites showing the maximum shear strains greater than 1% in downtown Mashiki. In Fig. 16, relationships between PGA on the ground surface and PBA (Peak Basement Acceleration) on the borehole at the strong-motion station of KiK-net KMMH16 during the 2016 Kumamoto earthquake sequence were shown. As for peak accelerations observed at the strong-motion station of KiK-net KMMH16, the non-linearity between the S-waves at the seismic bedrock and at the ground surface (Fig. 16c) was not clearly confirmed. In contrast, the non-linearity between the P-waves

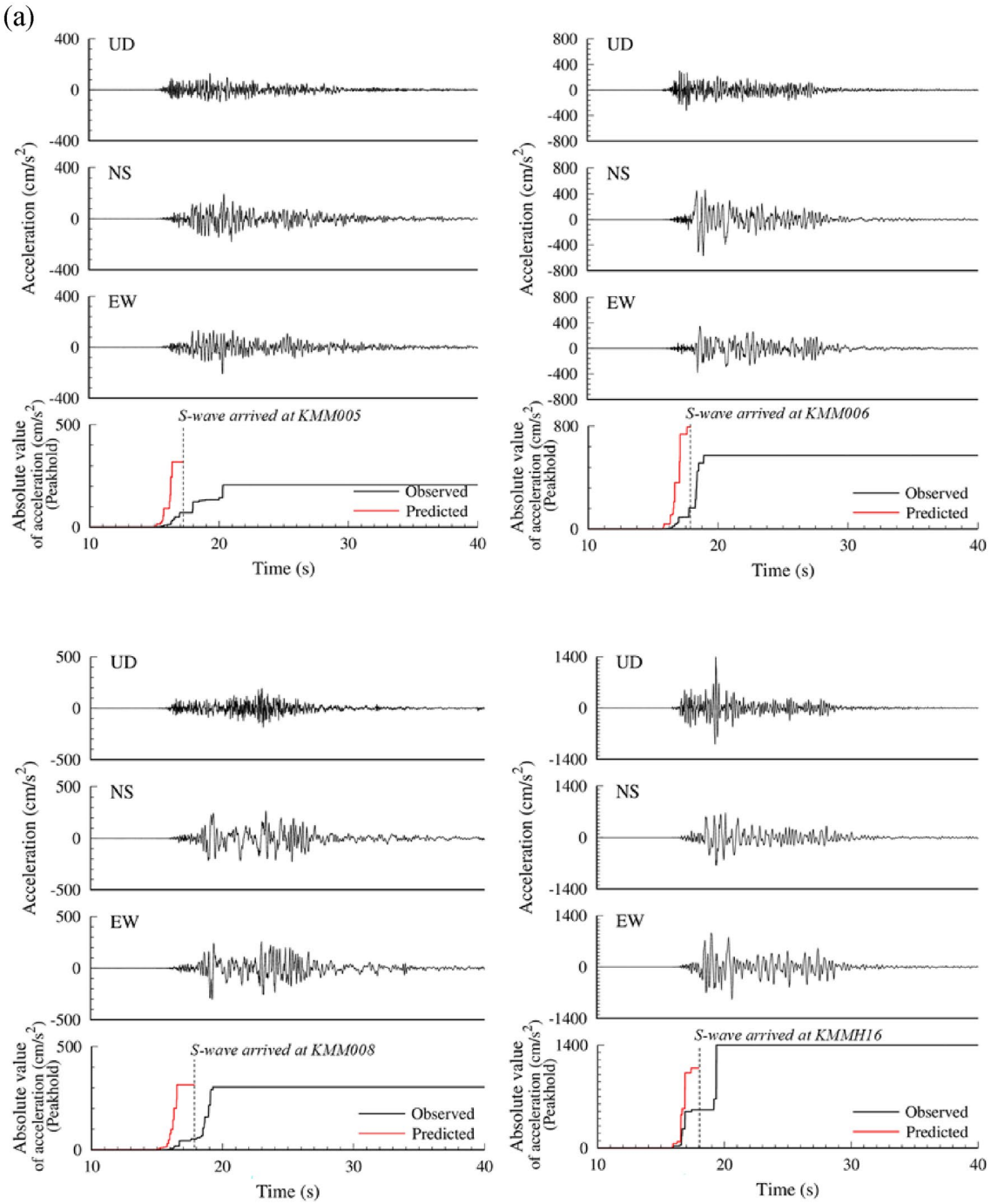

Fig. 15 Predicted and observed absolute values of accelerations (Peakhold) of S-waves at KMM005, KMM006, KMM008, and KMMH16, with the observed accelerations in 3 components during the 2016 Kumamoto earthquake sequence. Predicted absolute values of accelerations of S-waves by the method, are shown until the time that S-waves arrive at each station. **a** Foreshock (21:26 on April 14, *Mj* 6.5). **b** Mainshock (1:25 on April 16, *Mj* 7.3) **c** Largest aftershock (1:45 on April 16, *Mj* 5.9)

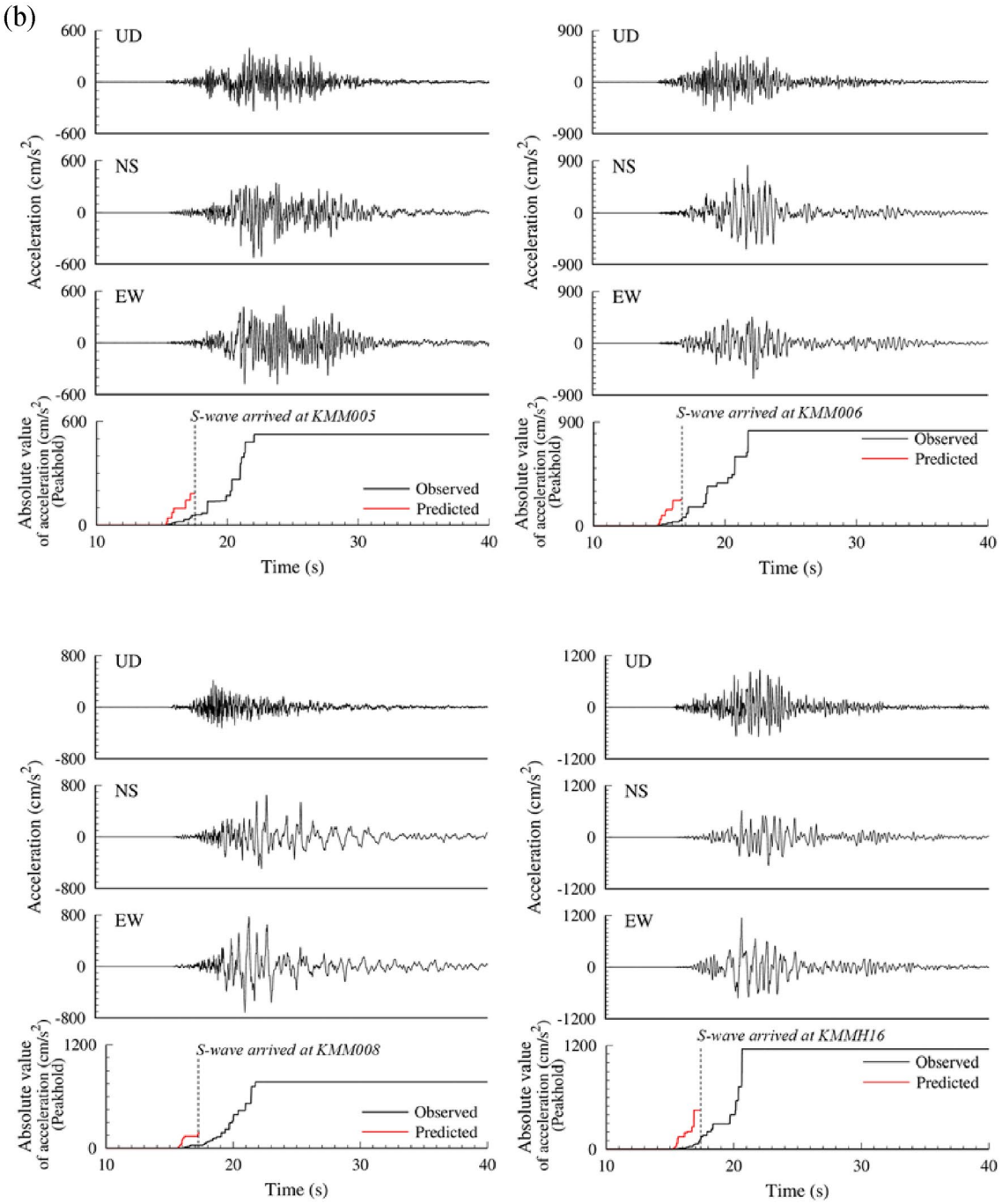

Fig. 15 continued

at the seismic bedrock and at the ground surface was clearly confirmed (Fig. 16b). The variability of the relationship between the P- and S-waves at the seismic bedrock (Fig. 16a) influenced by the source and path effects as shown in Eq. (3) was larger than the variability of the relationships between P-/S-waves at the seismic bedrock and

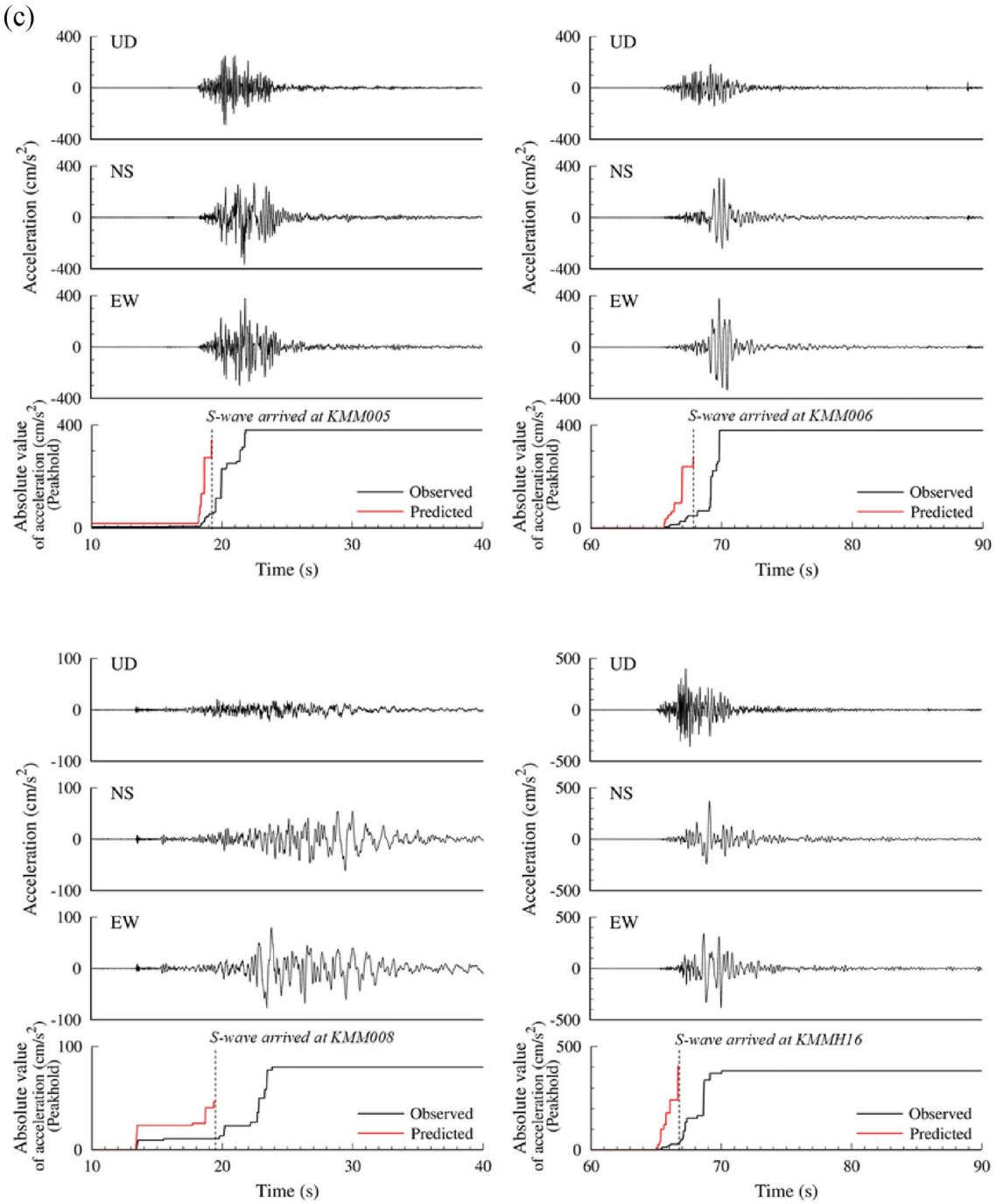

Fig. 15 continued

at the ground surface by the site effects. Therefore, this large variability hid the effect of the non-linearity of soil deposits. Finally, we could apply this method to the seismic data during the mainshock within the variability for the 2016 Kumamoto earthquake sequence (Fig. 16d).

Conclusions

This study investigated the applicability of the on-site P-wave earthquake early warning method based on the site-specific ratios of S-waves to P-waves for ground motions near an earthquake source fault region, using

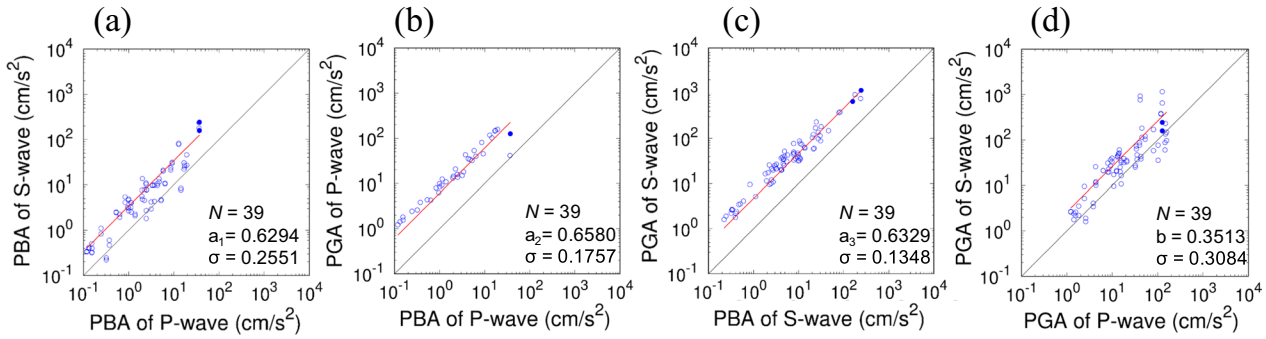

Fig. 16 Relationships between PGA (peak ground acceleration) on the ground surface and PBA (peak basement acceleration) on the borehole at the strong-motion station of KiK-net KMMH16, during the 2016 Kumamoto earthquake sequence. In the figure, standard deviation σ in logarithm is indicated, and closed circles indicate the mainshock. **a** PBA of S-wave and PBA of P-wave. **b** PGA of P-wave and PBA of P-wave. **c** PGA of S-wave and PBA of S-wave. **d** PGA of S-wave and PGA of P-wave

strong-motion data observed during the 2016 Kumamoto earthquake sequence in Japan. As a result, P-waves with a time-window length of 2.56 s after the arrival at most strong-motion stations were required at least to predict appropriately S-waves for the 2016 Kumamoto earthquake sequence, including the large-sized earthquakes. In cases of moderate-sized earthquakes as the foreshock (*Mj* 6.5) and largest aftershock (*Mj* 5.9), the proposed method can predict well the observed absolute accelerations despite the brief time until S-waves arrive at each station, mostly less than 2 s. In the case of large-sized earthquakes as the mainshock (*Mj* 7.3), the method can predict within a brief time of 0.5–2 s in the operational use that strong ground motions exceeding a certain threshold (e.g., acceleration of 150 cm/s^2) will come.

Non-linearity of soil deposits in the earthquake source fault region during the 2016 Kumamoto earthquake was reported by showing the maximum shear strains greater than 1% in downtown Mashiki. We found that the method was not strongly affected by the non-linearity of soil deposits due to strong ground motions during the 2016 Kumamoto earthquake sequence. The variability of the relationship between P- and S-waves at the seismic bedrock influenced by the source and path effects, is larger than the variability of the relationships between P-/S-waves at the seismic bedrock and at the ground surface by the site effects, and therefore, it hides the effect of the non-linearity of soil deposits.

Acknowledgements
We express our thanks to the National Research Institute for Earth Science and Disaster Resilience and JR Kyushu Railway Company, for providing us with strong-motion data.

Author contributions
ST and KN analyzed the strong-motion data. ST drafted the manuscript. All authors revised the manuscript. ST, MK, HY, KC, HM, NY authors participated in the temporary seismic observations.

Data availability statement
The data analyzed in this study is subject to the following licenses/restrictions: Original data is provided by NIED and JR-Kyushu. Requests to access the data analyzed should be directed to the corresponding author.

Declarations

Competing interests
The authors declare no competing financial interests.

Author details
[1]Railway Technical Research Institute, 2-8-38 Hikari-Cho, Kokubunji, Tokyo 185-5840, Japan. [2]JR Central Consultants Company, 2-1-95 Konan,Minato-Ku, Tokyo 108-0075, Japan. [3]Tokyo Institute of Technology, 4259 Nagatsuta,Midori-Ku, Yokohama, Kanagawa 227-8503, Japan. [4]Kagawa University, 1-1 Saiwai-Cho, Takamatsu, Kagawa 760-8521, Japan. [5]University of Tokyo, 1-1-1 Yayoi, Bunkyo-Ku, Tokyo 113-0032, Japan. [6]Kochi University, 2-5-1 Akebono-Cho, Kochi, Kochi 780-8520, Japan.

Received: 31 October 2022 Accepted: 19 January 2024
Published online: 18 February 2024

References

Allen RV (1978) Automatic earthquake recognition and timing from single traces. Bull Seismol Soc Am 68(5):1521–1532. https://doi.org/10.1785/BSSA0680051521

Allen RM, Kanamori H (2003) The potential for earthquake early warning in southern California. Science 300:786–789. https://doi.org/10.1126/science.1080912

Allen RM, Gasparini P, Kamigaichi O, Böse M (2009) The status of earthquake early warning around the world: an introductory overview. Seism Res Lett 80:682–693. https://doi.org/10.1785/gssrl.80.5.682

Asano K, Iwata T (2016) Source rupture processes of the foreshock and mainshock in the 2016 Kumamoto earthquake sequence estimated from the kinematic waveform inversion of strong motion data. Earth Planets Space 68:147. https://doi.org/10.1186/s40623-016-0519-9

Chimoto K, Yamanaka H, Tsuno S, Miyake H, Yamada N (2016) Estimation of shallow S-wave velocity structure using microtremor array exploration at temporary strong motion observation stations for aftershocks of the 2016 Kumamoto Earthquake. Earth Planets Space 68:206. https://doi.org/10.1186/s40623-016-0581-3

Field EH, Zeng Y, Johnson PA, Beresnev IA (1998) Nonlinear sediment response during the 1994 Northridge earthquake: observations and finite source simulations. J Geophys Res 103:26869–26883. https://doi.org/10.1029/98JB02235

Hoshizumi H, Ozaki M, Miyazaki K, Matsuura H, Toshimitsu S, Uto K, Uchiumi S, Komazawa M, Hiroshima T, Sudo S (2004) Geological map of Japan 1:200,000, Kumamoto. Geological Survey of Japan, AIST

Ishizaka S, Iwasaki Y, Hase Y, Watanabe K, Iwauchi A, Taziri M (1995) Subsidence and sediments of the last interglacial epoch in the Kumamoto Plain, Japan. Quat Res 34(5):335–344

Kawase H, Matsushima S, Nagashima F, Baoyintu NK (2017) The cause of heavy damage concentration in downtown Mashiki inferred from observed data and field survey of the 2016 Kumamoto earthquake. Earth Planets Space 69:3. https://doi.org/10.1186/s40623-016-0591-1

Kinoshita S (1998) Kyoshin Net (K-NET). Seismo Res Lett 69(4):309–332. https://doi.org/10.1785/gssrl.69.4.309

Matsubara M, Obara K (2011) The 2011 off the Pacific coast of Tohoku Earthquake related to a strong velocity gradient with the Pacific plate. Earth Planets Space 63:663–667. https://doi.org/10.5047/eps.2011.05.018

Matsubara M, Hayashi H, Obara K, Kasahara K (2005) Low-velocity oceanic crust at the top of the Philippine Sea and Pacific plates beneath the Kanto region, central Japan, imaged by seismic tomography. J Geophys Res 110:B12. https://doi.org/10.1029/2005JB003673

Miyakoshi H, Tsuno S (2015) Influence of the source, path and site effects on the relationship between P-waves at the seismic bedrock and S-waves on the ground surface – for the application to the on-site earthquake early warning. Zisin 68:91–105. https://doi.org/10.4294/zisin.68.91(inJapanesewithEnglishabstract)

Miyakoshi H, Tsuno S, Chimoto K, Yamanaka H (2019) Investigation of site amplification factors for S- and P-waves from spectral inversions in the Tokyo metropolitan area, Japan – for application to earthquake early warnings. J Seismol 23:561–578. https://doi.org/10.1007/s10950-019-09823-4

Morita Y, Hamaguchi H (1981) Automatic detection of S-onset times using two dimensional autoregressive model fitting. Zisin 34(2):223–240. https://doi.org/10.4294/zisin1948.34.2_223(inJapanesewithEnglishabstract)

Nakamura Y (1988) On the urgent earthquake detection and alarm system (UrEDAS). Proc. of 9th World Conference on Earthquake Engineering 7:673–678.

National Research Institute for Earth Science and Disaster Resilience (2019a) J-SHIS Japan Seismic Hazard Information Station. https://doi.org/10.17598/nied.0010

National Research Institute for Earth Science and Disaster Resilience (2019b) NIED K-NET, KiK-net. https://doi.org/10.17598/NIED.0004

Odaka T, Ashiya K, Tsukada S, Sato S, Ohtake K, Nozaka D (2003) A new method of quickly estimating epicentral distance and magnitude from a single seismic record. Bull Seism Soc Am 93(1):526–532. https://doi.org/10.1785/0120020008

Okamoto K, Tsuno S (2015) Investigation on relationship between epicentral distance and growth curve of initial P-wave propagating in local heterogeneous media for earthquake early warning system. Earth Planets Space 67:167. https://doi.org/10.1186/s40623-015-0339-3

Sun J, Nagashima F, Kawase H, Matsushima S, Baoyintu (2021) Simulation of building damage distribution in downtown Mashiki, Kumamoto, Japan caused by the 2016 Kumamoto earthquake based on site-specific ground motions and nonlinear structural analyses. Bull Earthq Eng 19:3491–3521. https://doi.org/10.1007/s10518-021-01119-8

Sun J, Kawase H, Fukutake K, Nagashima F, Matsushima S (2022) Simulation of soil liquefaction distribution in downtown Mashiki during 2016 Kumamoto earthquake using nonlinear site response. Bull Earthq Eng 20:5633–5675. https://doi.org/10.1007/s10518-022-01426-8

Suzuki W, Aoi S, Kunugi T, Kubo H, Morikawa N, Nakamura H, Kimura T, Fujiwara H (2017) Strong motions observed by K-NET and KiK-net during the 2016 Kumamoto earthquake sequence. Earth Planets Space 69:19. https://doi.org/10.1186/s40623-017-0604-8

Tsuno S (2021) Applicability of on-site P-wave earthquake early warning to seismic data observed during the 2011 off the Pacific coast of Tohoku earthquake, Japan. Front Earth Sci 9:681199. https://doi.org/10.3389/feart.2021.681199

Tsuno S, Miyakoshi H (2019) Investigation of earthquake warning for the threshold of P-wave, using an amplitude ratio of S-wave to P-wave. Journal of JAEE 19(6):105–115. https://doi.org/10.5610/jaee.19.6_105

Tsuno S, Korenaga M, Okamoto K, Yamanaka H, Chimoto K, Matsushima T (2017) Local site effects in Kumamoto City revealed by the 2016 Kumamoto earthquake. Earth Planets Space 69:37. https://doi.org/10.1186/s40623-017-0622-6

Wakamatsu K, Senna S, Ozawa K (2017) Liquefaction and its characteristics during the 2016 Kumamoto earthquake. J JAEE 17(4):81–100. https://doi.org/10.5610/jaee.17.4_81

Wu YM, Kanamori H (2005) Rapid assessment of damaging potential of earthquakes in Taiwan from the beginning of P waves. Bull Seism Soc Am 95(3):1181–1185. https://doi.org/10.1785/0120040193

Wu YM, Kanamori H, Allen RM, Hauksson E (2007) Determination of earthquake early warning parameters, τ_c and P_d, from southern California. Geophys J Int 170:711–717. https://doi.org/10.1111/j.1365-246X.2007.03430.x

Yamada M, Ohmura J, Goto H (2017) Wooden building damage analysis in Mashiki town for the 2016 Kumamoto earthquakes on April 14 and 16. Earthq Spectra 33(4):1555–1572. https://doi.org/10.1193/090816eqs144m

Yamanaka H, Chimoto K, Miyake H, Tsuno S, Yamada N (2016) Observation of earthquake ground motion due to aftershocks of the 2016 Kumamoto earthquake in damaged areas. Earth Planets Space 68:197. https://doi.org/10.1186/s40623-016-0574-2

Zhao C, Zhao JX (2019) S- and P-wave spectral ratios for on-site earthquake early warning in Japan. Bull Seism Soc Am 109(1):395–412. https://doi.org/10.1785/0120180116

Publisher's Note